Enhanced nonlinear spectroscopy for monolayers and thin films in near-Brewster's angle reflection pump-probe geometry

Jun Nishida, Chang Yan, and Michael D. Fayer[a)]
Department of Chemistry, Stanford University, Stanford, California 94305, USA

(Received 10 January 2017; accepted 7 February 2017; published online 7 March 2017)

We experimentally demonstrate and theoretically explicate a method that greatly enhances the detection of third-order nonlinear signals from monolayers and thin films on dielectric substrates. Nonlinear infrared signals, including two dimensional infrared (2D IR) vibrational echo signals, were detected from a functionalized alkyl chain monolayer on a dielectric SiO_2 surface in a near-Brewster's angle reflection pump-probe geometry. We observed a tremendous enhancement of the signal-to-noise (S/N) ratio in this geometry compared with a conventional transmission pump-probe geometry signal. The S/N enhancement is achieved by the greatly increased modulation of the local oscillator (LO) field that is induced by the nonlinear signal field. By reducing the LO field without loss of the signal field, the modulation amplitude acquired in this geometry was enhanced by more than a factor of 50. The incident angle dependence of the enhancement was measured and the result agreed remarkably well with theoretical calculations. We combined this geometry with a germanium acousto-optic modulator pulse shaping system to apply 2D IR spectroscopy to the monolayer. The enhanced and phase-stable 2D IR spectra gave detailed dynamical information for the functionalized alkyl chain monolayer. The application of the method to films with finite thickness was described theoretically. The range of film thicknesses over which the method is applicable is delineated, and we demonstrate that accurate dynamical information from thin films can be obtained in spite of dispersive contributions that increase with the film thickness. While we focus on infrared experiments in this article, the method and the theory are applicable to visible and ultraviolet experiments as well. *Published by AIP Publishing.* [http://dx.doi.org/10.1063/1.4977508]

I. INTRODUCTION

Ultrafast nonlinear spectroscopy has been established as a powerful technique for studying the dynamics of complex molecular systems.[1–5] Third-order infrared experiments, such as two dimensional infrared (2D IR) spectroscopy, have been particularly successful in elucidating sub-picosecond to nanosecond dynamics occurring in a variety of condensed phase materials.[6–14] These third-order spectroscopic methods require three time-sequenced input pulses with electric fields E_1, E_2, and E_3 to generate a third-order nonlinear polarization $P^{(3)} = \varepsilon_0 \chi^{(3)} E_1 E_2 E_3$, which emits a nonlinear signal field, E_{sig}. The emitted signal is heterodyned (interfered) with a local oscillator (LO) pulse with electric field E_{LO}. In a 2D IR experiment, the heterodyne detection provides necessary phase information to perform Fourier transformation from the time domain into the frequency domain.

In third-order nonlinear infrared spectroscopy, the pump-probe geometry is the simplest geometry to implement. The first two "pump" pulses (E_1, E_2) are collinear, and the third "probe" pulse (E_3) intersects the pump pulses at a small angle.[15] In this geometry, E_{sig} is emitted collinearly with the probe pulse, and the probe pulse serves as a local oscillator as well. Compared with a fully non-collinear geometry, the pump-probe geometry has an advantage in terms of its inherent phase-stability[16] and its compatibility with a germanium acousto-optic modulator (AOM) pulse shaping system,[15,17] which significantly accelerates the data acquisition rate in 2D IR spectroscopy.[18,19] The signal and the LO have a well-defined fixed phase relationship with no ambiguity, and therefore numerical post-processing referred to as "phasing" is unnecessary in the pump-probe geometry implemented with an AOM pulse shaping system.

The disadvantage of the pump-probe geometry is the lack of sensitivity arising from its inability to adjust the local oscillator amplitude E_{LO} relative to the signal amplitude E_{sig}.[18] The pulse that is observed by an intensity detector is $|E_{LO} + E_{sig}|^2 = |E_{LO}|^2 + |E_{sig}|^2 + 2\mathrm{Re}[E_{LO} \cdot E_{sig}{}^*]$. $|E_{sig}|^2$ is too small to be detected. In an experiment, $|E_{LO}|^2$ is subtracted and the result is divided by $|E_{LO}|^2$, yielding $2\mathrm{Re}[E_{LO} \cdot E_{sig}{}^*]/|E_{LO}|^2$. This is the modulation in the LO intensity induced by the signal field. The heterodyned modulation (the "heterodyned signal") is thus essentially proportional to E_{sig}/E_{LO}. Therefore when E_{sig} is small, E_{LO} should be reduced so that E_{sig}/E_{LO} is increased. The reduction in E_{LO} will improve the signal-to-noise (S/N) ratio until the detector noise becomes a dominant noise source. This adjustment of the local oscillator amplitude is straightforward in a fully non-collinear geometry with an external local oscillator.[20] In the pump-probe geometry, however, the third pulse is itself the local oscillator ($E_3 = E_{LO}$), and the attenuation of E_3 leads to a reduction of E_{sig} by the exact same fraction, rendering E_{sig}/E_{LO} invariant.

a)Telephone: 650 723-4446. Electronic mail: fayer@stanford.edu.

When bulk liquids are measured, E_{sig} is often large enough that the advantage of the pump-probe geometry is not compromised by the reduced sensitivity.[18] However, the lack of the sensitivity is particularly an issue when a molecular monolayer or a thin film is studied, for which the nonlinear signals are orders of magnitude smaller compared to bulk samples.[21,22] E_{sig} itself can be enhanced if sample films are coated on metallic and/or nano-structured surfaces,[23–25] but many interesting monolayers and films involve flat dielectric surfaces[21,26–30] for which such an approach is not applicable.

A few methods have been suggested to reduce the local oscillator field in the pump-probe geometry, including the use of a polarization grating configuration[31] or a Sagnac interferometer.[32] In the context of two-dimensional infrared/near-infrared spectroscopy, these methods have so far yielded up to a factor of ~5 enhancement in heterodyned signals. While the enhancement is significant, a further enhancement is necessary to readily apply 2D IR and other nonlinear spectroscopies to monolayer and thin film samples.

In this report, we demonstrate that, for molecular monolayers or thin films at dielectric interfaces, the signal in the pump-probe geometry is significantly enhanced in the reflection mode rather than the conventional transmission mode (see Figure 1(a)). A particularly large enhancement in a heterodyned signal can be achieved when the probe pulse is *p*-polarized and the incident angle of the probe pulse is close to the Brewster's angle, so that only a small fraction of the probe pulse is reflected. The small reflection can be regarded as a LO field that is heavily attenuated. Although the LO field is greatly reduced, the signal field induced by pulse 3 is not reduced, so the ratio, E_{sig}/E_{LO}, can be increased substantially.

II. RESULTS AND DISCUSSION

A. Reflection mode pump-probe spectroscopy on a molecular monolayer

To develop and quantitatively investigate the methodology, we employed the near-Brewster's angle reflection pump-probe geometry to study the C_{11}-alkylsiloxane monolayer functionalized with a rhenium metal carbonyl complex, Re(phen) $(CO)_3Cl$; the alkyl chains are bound to a thin SiO_2 film (100 nm) on a CaF_2 substrate.[21,33,34] The symmetric CO stretch mode (2022 cm^{-1}) of the metal carbonyl head group is used as the vibrational probe.

A schematic illustration of the experimental geometry is given in Figure 1(a) for a pump-probe experiment, where one pump pulse induces two simultaneous interactions between the pump pulse field and the sample's transition dipole moments. (For 2D IR experiments discussed later, the pump pulse is split into two temporarily separated pulses.) We set both the pump and probe polarizations to *p*-polarizations, and the crossing angle between the pump and probe pulses was 20°. Note that the probe polarization has to be *p*-polarized to achieve the large enhancement discussed below because the reflection vanishes at the Brewster's angle only for *p*-polarization. *s*-polarization can also give substantial enhancement but significantly less than *p*-polarization (see Figure S2 of the supplementary material).[35] The probe incident angle θ_i is variable. The sample layer lies between air (n_1 = 1) and SiO_2/CaF_2 substrate

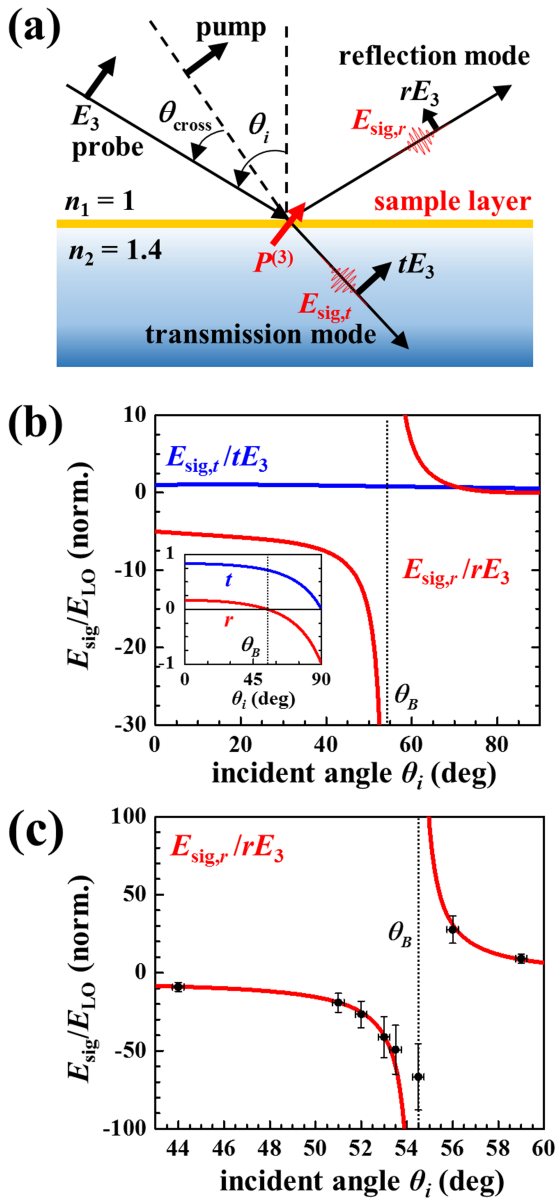

FIG. 1. (a) Schematic illustration of the pump-probe experiment for a monolayer on a SiO_2/CaF_2 (n_2 = 1.4) substrate. The monolayer is functionalized with a rhenium metal carbonyl complex. The *p*-polarized pump and probe pulses generate a third-order nonlinear polarization in the monolayer, which emits signal fields $E_{sig,r}$ (reflected) and $E_{sig,t}$ (transmitted). These emitted signals are heterodyned by the reflected probe (rE_3) and transmitted probe (tE_3), respectively. The incident angle θ_i is variable, while the crossing angle θ_{cross} was fixed to 20°. (b) Calculated θ_i dependence of the heterodyned pump-probe signal amplitudes (E_{sig}/E_{LO}) for both transmission mode ($E_{sig,t}/tE_3$) and reflection mode ($E_{sig,r}/rE_3$). The signals are normalized by $E_{sig,t}/tE_3$ at $\theta_i = 0°$. $E_{sig,r}/rE_3$ diverges near Brewster's angle ($\theta_B = 54.5°$). Inset: Fresnel reflection (r) and transmission (t) coefficients. (c) Red solid curve: calculated $E_{sig,r}/rE_3$ near Brewster's angle, $\theta_B = 54.5°$. Black circles: experimental enhancement factors based on the data in Figure 2(b). The calculation agrees well with the experimentally measured enhancement factors. Error bars: 1 standard deviation error in the experimental enhancement factors, mainly arising from the uncertainty in the amplitude of the small transmission mode signal (Figure 2(b), inset).

(n_2 = 1.4).[34] First, a pump pulse crosses the sample layer, and after time t, a probe pulse is incident. The probe beam is partially reflected and transmitted. The field reflection/transmission coefficients with respect to θ_i are plotted in the inset of Figure 1(b). At the Brewster's angle θ_B = 54.5°,

r = 0; there is no reflection. The pump and probe pulses together induce a third-order nonlinear polarization which emits signal fields in both the reflected and transmitted probe directions. These signal fields are denoted as $E_{sig,r}$ and $E_{sig,t}$, respectively. The signal fields are heterodyned by the reflected and transmitted probe pulses, namely, rE_3 and tE_3. Therefore, the modulation in the local oscillator field observed in the reflection mode is $\sim E_{sig,r}/rE_3$, while in the transmission mode the modulation is $\sim E_{sig,t}/tE_3$. In the following discussion, $E_{sig,r}/rE_3$ and $E_{sig,t}/tE_3$ are referred to as "heterodyned modulation" or "heterodyned signal," while $E_{sig,r}$ and $E_{sig,t}$ are referred to as "signal fields." The heterodyned signals are observed as pump-probe signals in the experiments. Note that the incident angle dependences of the local oscillators (rE_3, tE_3) and the signal fields ($E_{sig,r}$, $E_{sig,t}$) are determined by fundamentally different physical mechanisms. The reflected/transmitted local oscillator fields, rE_3 and tE_3, are determined by polarizations non-resonantly induced by E_3 in the substrate (Figure 1(b), inset).[35] On the other hand, $E_{sig,r}$ and $E_{sig,t}$ are radiated from the resonantly induced polarization sheet lying between the air and the substrate. In a thick bulk sample, the signal radiation from resonantly induced polarization will constructively interfere only in the transmission direction. However, in the monolayer studied here, with thickness much smaller than the infrared wavelength, the signal radiation constructively interferes in the reflection direction as well. As a result, $E_{sig,r}$ and $E_{sig,t}$ are comparable in amplitude, and both of the signal fields remain finite near the Brewster's angle.

The incident angle θ_i dependence of the reflection mode heterodyned modulation ($E_{sig,r}/rE_3$) and the transmission mode heterodyned modulation ($E_{sig,t}/tE_3$) was calculated based on the orientational distribution of the vibrational probes' transition dipoles reported previously.[34] The results are shown in Figures 1(b) and 1(c). Note that the signals are normalized by $E_{sig,t}/tE_3$ at $\theta_i = 0°$, i.e., a conventional transmission pump-probe signal with normal incidence. The calculation details are given in the supplementary material, which includes discussions of the other possible combinations of the pump/probe polarizations (Figures S1 and S2).[36–40] As seen in Figure 1(b), at θ_i = 0°, the heterodyned signal in the reflection mode is opposite in phase from the signal in the transmission mode; while $E_{sig,r}$ and $E_{sig,t}$ are in-phase, rE_3 and tE_3 are 180° out-of-phase, resulting in the opposite signs of the heterodyned signals. At θ_i = 0°, $E_{sig,r}/rE_3$ is a factor of ~5 larger than $E_{sig,t}/tE_3$ in amplitude because r is smaller than t by a factor of ~5 (Figure 1(b), inset) while $|E_{sig,r}| \approx |E_{sig,t}|$. As θ_i increases, the signal in the transmission mode ($E_{sig,t}/tE_3$) gently decreases due to orientational and geometrical factors, including the number of molecules in the focus and local field effects (see Eq. S(6) in the supplementary material). However, the signal in the reflection mode ($E_{sig,r}/rE_3$) rapidly grows in amplitude and then diverges to negative infinity near the Brewster's angle because r approaches zero and $E_{sig,r}$ remains finite. Once the incident angle θ_i exceeds the Brewster's angle, r flips its sign and rE_3 and tE_3 are in-phase. Therefore, when the incident angle θ_i is slightly above the Brewster's angle, the heterodyned signal in the reflection mode is positively enhanced. As the incident angle further increases, $E_{sig,r}/rE_3$ decreases due to the increasing rE_3.

The configuration in Figure 1(a) was experimentally implemented to acquire pump-probe signals in both transmission and reflection modes (Figure S3). The pump-probe signals were recorded as $(I_{on} - I_{off})/I_{off}$, where I_{on} and I_{off} are probe intensities with and without a pump pulse. Depending on the detection mode and the incident angle, the probe intensities recorded on a HgCdTe array detector were vastly different as seen in the inset of Figure 1(b). When the array detector was saturated by high infrared intensity, a neutral density filter was placed in front of the entrance slit of the spectrograph (see the supplementary material for details).

Figure 2(a) shows pump-probe spectra acquired at t = 20 ps with a normal ($\theta_i = 0°$) transmission mode and the near-Brewster's angle reflection mode. Compared with the conventional transmission pump-probe signal, near-Brewster's angle reflection pump-probe signals are significantly enhanced. When θ_i is slightly below θ_B, the signal

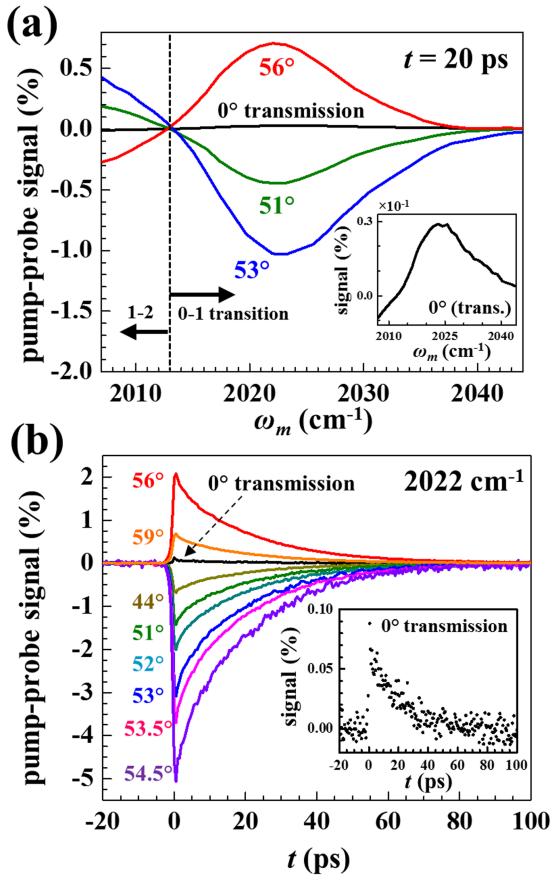

FIG. 2. (a) Reflection mode pump-probe spectra recorded at t = 20 ps with three incident angles, 51°, 53°, and 56°. A transmission mode spectrum (normal incidence) is also included and shown with a greatly expanded scale in the inset. The signal is greatly enhanced in the reflection geometry. For all the spectra, the features at >2013 cm^{-1} arise from 0-1 transition, while the features at <2013 cm^{-1} arise from 1-2 transition. When the reflection mode probe incident angle is less than the Brewster's angle, the signals are opposite in sign from the transmission mode signal. (b) Pump-probe decays in the reflection geometry recorded at the frequency of 2022 cm^{-1} and with various incident angles. The signals were averaged over 40 min for each incident angle. The very small transmission data are also shown (inset, expanded scale). The very large signal enhancement and improved data quality in the reflection geometry are clearly evident.

arising from 0-1 transition is strongly negatively enhanced, while it is positively enhanced for θ_i slightly above θ_B. This qualitative behavior perfectly agrees with the theoretical prediction in Figures 1(b) and 1(c). The 1-2 transition signals are opposite in phase from 0-1 transition signals.[41]

Figure 2(b) shows the time t dependence of the pump-probe signal recorded at the band center, 2022.0 cm^{-1}. Compared with the conventional normal pump-probe signal, the enhancement in the pump-probe signal amplitudes and the drastic improvements in the S/N ratios are obvious. The pump-probe signal decays in time due to the population decay and the in-plane/out-of-plane reorientation of the head groups.[34,40] All the signals were fit well with the bi-exponential decays with the time constants of 1.8 ps (~25%) and 21 ps (~75%). The signals were extrapolated to $t = 0$ based on the fit and normalized by the normal transmission pump-probe signal to yield the enhancement factor. The results are plotted in Figure 1(c) as circles. The observed enhancement factor agrees remarkably well with the calculated enhancement factor, verifying that we properly formulated the enhancement mechanism and correctly characterized the orientational distribution of the head groups in our previous publication.[34] Right at or very near the Brewster's angle (θ_i = 54.5°), the reflected probe is significantly contaminated with s-polarization because the reflection coefficient for s-polarization is orders of magnitude higher than that for p-polarization near the Brewster's angle.[35] A small degree of contamination by s-polarization in the incident probe beam is then very significant in the reflected probe beam. The contamination by s-polarization in the probe prevents the enhancement factor from diverging (Figure S2 of the supplementary material).

While a large enhancement due to a small reflection is advantageous when the noise is dominated by laser fluctuations, a reflection that is too small is disadvantageous once detector noise becomes dominant. Overall the best signal-to-noise ratio was achieved when θ_i was set to 53.5°. As one of the advantages of this geometry, the local oscillator amplitude can be readily optimized by adjusting the incident angle of the probe beam.

In this geometry, even a linear infrared signal is enhanced.[28–30] The phase of the absorption depends on the incident angle, and a strongly enhanced negatively going absorption was observed when the incident angle was set slightly smaller than the Brewster's angle (Figures S5B and S5C of the supplementary material). The enhanced pump-probe signals observed here can be viewed as the modulation of the enhanced probe absorptions induced by the pump pulse.

B. Reflection mode 2D IR spectroscopy on a monolayer

Based on the pump-probe geometry shown in Figure 1(a), 2D IR spectra can be acquired as well by splitting a pump pulse into two temporarily separated collinear pulses.[4,15] The temporal separation between the two pump pulses is denoted as τ, and the waiting time between the second pump pulse and the probe pulse is denoted as T_w. The two collinear pump pulses were generated as outputs from a Ge-AOM pulse shaper. As τ is scanned, a pump-probe spectrum as in Figure 2(a) is modulated for each optical frequency ω_m, and Fourier transform of the acquired interferograms yields the ω_τ axis of the 2D spectrum. The phases of the two pump pulses were altered with a four-shot phase cycling scheme to extract the vibrational echo signal.[15]

The 2D IR signal amplitude is proportional to the pump-probe signal amplitude, and therefore the 2D IR signal is enhanced by the exact same enhancement factors shown in Figures 1(b) and 1(c) (see Figure S4 of the supplementary material). Figure 3 shows three 2D IR spectra with the same waiting time T_w = 10 ps but with different detection modes: transmission (0°) and reflection with two different incident angles (53.5° and 56°). Red is positive going and blue is negative going. The transmission mode spectrum is positive going centered around 2022 cm^{-1}. The reflection mode spectrum with the angle slightly less than the Brewster's angle (53.5°) is negative going. When the angle is increased slightly past the Brewster's angle (56°), the signal changes its sign and is positive going. This change in sign is equivalent to the change observed in the pump-probe data shown in Figure 2. Below the

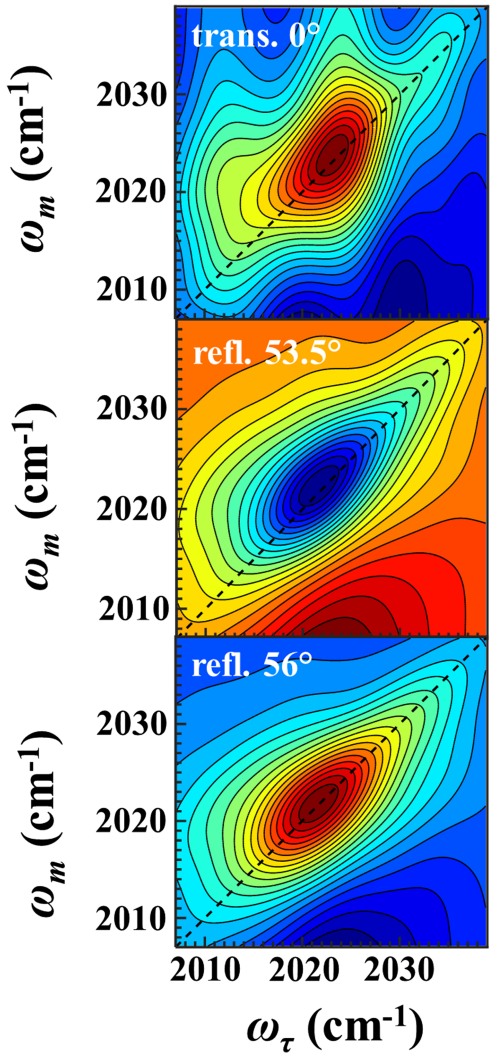

FIG. 3. 2D IR spectra with the waiting time T_w = 10 ps recorded in the transmission mode (top) and in the reflection mode with θ_i = 53.5° (middle) and θ_i = 56° (bottom). For θ_i less than Brewster's angle, the sign of the reflection mode spectrum (middle) is opposite of the transmission mode spectrum (top). When θ_i is greater than Brewster's angle (bottom) the sign is the same as in the transmission mode. The data quality is far superior in the reflection mode.

main bands (around $\omega_m = 2022\ \mathrm{cm}^{-1}$), which arise from the 0-1 transition, a portion of the bands with the echo emission at the 1-2 transition frequency can be seen with opposite signs from the main bands. The drastic improvement in the S/N ratio for the reflection mode signals is obvious. Based on 5 min scans of the interferograms (Figure S4 of the supplementary material), the S/N ratio for the 53.5° reflection mode data was estimated to be a factor of ~20 greater compared to the transmission mode data. Assuming that the noise is random Gaussian fluctuations, to obtain the same S/N in the transmission mode would take 400× longer.

The observed band shape of the 2D IR spectra contains the dynamical information of the monolayer. Here, we briefly provide an intuitive interpretation of the 2D IR spectra. The linear absorption spectrum of the vibrational probe is inhomogeneously broadened. At a given instant of time, different vibrational probes will have distinct frequencies within the inhomogeneous line because of diverse structural environments that give rise to different intermolecular interactions. As time proceeds, the structure of the medium evolves, causing the vibrational frequencies to change. The time evolution of the frequencies is called spectral diffusion. The time dependence of the spectral diffusion directly reflects the dynamical evolution of the structure. A 2D IR spectrum shows the correlation between the initial (ω_τ) and final (ω_m) frequencies separated by the waiting time T_w. When T_w is short, the two frequencies are nearly the same because the system has not undergone significant structural changes. The correlation between the initial and final frequencies is manifested as a 2D spectrum that is elongated along the diagonal. At sufficiently long T_w, structural dynamics will have sampled all configurations that give rise to the probe vibrational frequencies. As a result the frequencies have been randomized, rendering ω_τ and ω_m uncorrelated. The lack of correlation at long T_w yields an essentially round 2D band shape. Thus, by tracking the evolution of the 2D band shape with respect to T_w, the structural dynamics of the system can be determined.

2D IR spectra were acquired at varieties of T_w, and each of the two-dimensional band shapes was quantitatively evaluated using the center line slope (CLS) method.[42,43] The CLS(T_w) decay curve is the normalized frequency-frequency correlation function (FFCF).[42]

CLS decays acquired in the reflection mode are plotted in Figure 4(a), together with a decay acquired in the transmission mode (inset). The data for both the reflection and transmission modes are plotted up to 40 ps. The reflection mode data for a variety of probe pulse incident angles are shown. It is clear that the CLS decays in the reflection mode are independent of the incident angle of the probe pulse.

Note that the heterodyned 2D IR signal amplitude decays with increasing T_w due to the reorientation and vibrational relaxation of the vibrational probe. The decaying time constant is identical to the pump-probe signal in Figure 3 (middle panel) (~20 ps). Therefore, as T_w is increased, the heterodyned 2D IR signal decreases in amplitude, leading to a lower S/N ratio when the band shape is evaluated by the CLS method. The transmission mode data (inset) could be taken only up to 40 ps (~2 lifetimes) due to the small heterodyned signal amplitude. In contrast, reflection mode 2D IR spectra were

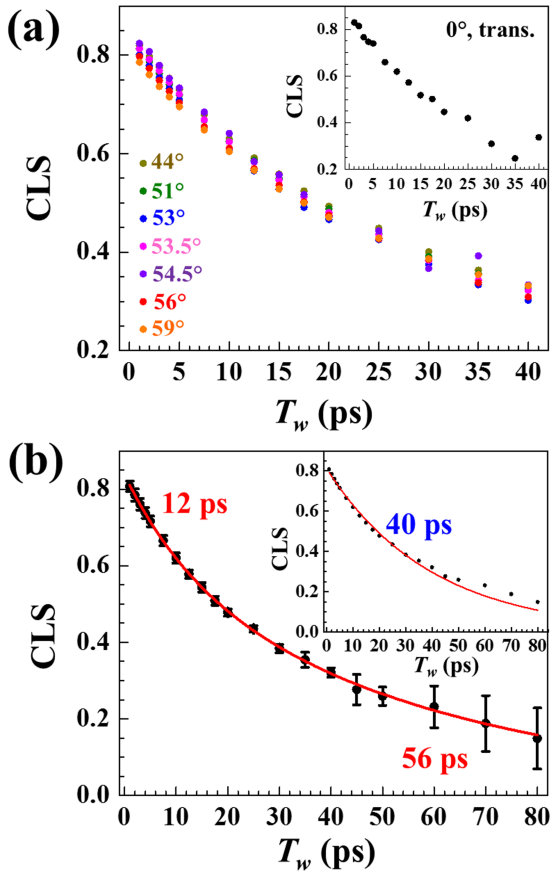

FIG. 4. (a) Monolayer CLS decays obtained from reflection mode 2D IR spectra with various incident angles up to T_w = 40 ps. The CLS(T_w) decays were taken over 12 h for each incident angle. The CLS decays are independent of the probe incident angle. Inset—a CLS decay acquired from transmission mode 2D IR spectra with normal incidence. (b) The average of the CLS decays acquired in the reflection mode plotted up to 80 ps. Error bars are 1 standard deviation. Red solid curve: a biexponential fit with the two time constants of 12 ± 2 ps and 56 ± 5 ps. Inset: the same data fit with a single exponential (red curve) with the time constant of 40 ± 1 ps.

able to be acquired up to 80 ps (~4 lifetimes) due to the signal enhancement, making it possible to monitor the dynamical evolution in a wider temporal window. To reduce the error bars on the data, particularly at the long T_w points, all the CLS decays acquired in the reflection mode were averaged and plotted in Figure 4(b) with 1 standard deviation error bars up to 80 ps.

The same sample was previously studied with 2D IR spectroscopy in BOXCARS geometry.[33] Owing to an adjustable external local oscillator, the heterodyned signal was relatively large (~1% modulation). However, the data quality was limited by the slow data acquisition rate due to motions of mechanical delay lines, chopping, and the need for post-acquisition numerical data processing to account for the uncertainty in the relative phase relationship between the signal and the external local oscillator.[20] Note that all of these problems are overcome in the pump-probe geometry.[15,18] The data from the BOXCARS geometry with limited data quality and time range were fit as a single exponential decay with the time constant of 38 ± 1 ps.[33] When the data acquired here in the reflection mode pump-probe are fit with a single exponential (Figure 4(b), inset), the fit yielded a time constant of 40 ± 1 ps. The time

constant agrees well with the result from the BOXCARS geometry. However, with the high quality data in Figure 4(b), it is clear that the single exponential fit is not fitting the entire decay well. Instead, the data were fit very well with a biexponential function with the two time constants of 12 ± 2 ps and 56 ± 5 ps (Figure 4(b), main panel).

The time constants from the biexponential fit of 12 ps and 56 ps reflect spectral diffusion time constants that arise from dynamics occurring on different time scales in the monolayer. We recently observed two distinct time scales in the in-plane reorientation of the head groups as well.[34] MD simulations of the same functionalized chains but on a crystalline gold substrate showed a number of processes, such as the formation of gauche defects in the alkyl chains, occurring on different time scales.[22] The simulations reproduced the experimental CLS decays from the BOXCARS geometry very well, but the limited time range of the CLS data hampered the observations of the detailed dynamical processes. Here, with the enhanced data quality, we were able to observe the multiple time scale chain dynamics predicted by the MD simulations.

C. Application to thin films: Theory

The application of the near-Brewster's angle reflection pump-probe geometry to monolayer samples was experimentally demonstrated above. Another promising application of this method is the study of thin films deposited on dielectric media (Figure 5(a)).[26,27] If the film is thin enough, the enhancement technique demonstrated above is applicable to the film as well. The questions are as follows: (1) to what extent and under what conditions is a signal enhanced for a film with finite thickness, and (2) do the acquired two-dimensional spectra in 2D IR experiment yield the correct dynamics. In the following, these issues are theoretically investigated.

In Figure 5(a), the top layer is air ($n_1 = 1$) and the third layer is a transparent dielectric ($n_3 = 1.4$). The second sample layer is three-dimensionally isotropic and has a vibrational probe that resonantly absorbs the incident IR beams. For example, the second layer could be a thin film consisting of randomly orientated crystals functionalized with vibrational probes. Due to the resonant absorption, the refractive index for the second layer is complex $n_2 + ik_2$. We assume that the real part of the second layer's refractive index is matched with the third layer, i.e., $n_2 = n_3 = 1.4$. The IR probe beam propagating in the layer induces a $P_i^{(3)}$ polarization at a certain location i in the layer, and $P_i^{(3)}$ emits a signal field $E_{r,i}^{sig}$ in the reflected probe direction. The signal detected is the sum of the signal fields from all the positions in the layer: $E_r^{sig} = \sum_i E_{r,i}^{sig}$. Depending on where in the layer a molecule is excited, the phase of $E_{r,i}^{sig}$ varies. Therefore the signal fields from different positions in the layer do not add up in-phase. The overall signal field E_r^{sig} gradually shifts in phase as the thickness grows and therefore the dispersive line shape (~Re[$\chi^{(3)}$]) starts contributing to the signal field in addition to the absorptive line shape (~Im[$\chi^{(3)}$]). If the sample is sufficiently thick, the signal field from deep in the film will be phase shifted sufficiently to destructively interfere with the signal field generated near the surface of the sample, limiting the thickness of the sample to which the method can be applied.

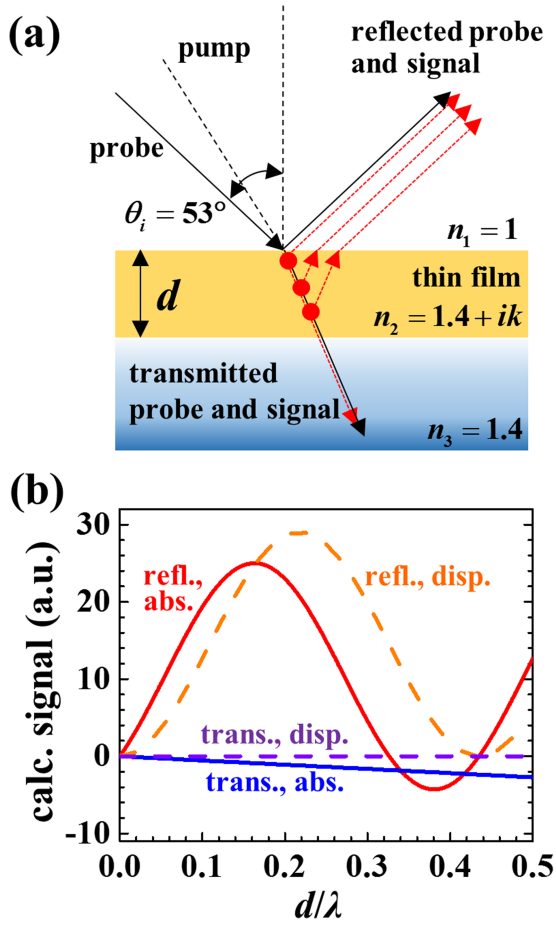

FIG. 5. (a) Schematic illustration of the pump-probe experiment on a film with finite thickness. The second layer with the thickness d is the sample thin film. For the calculations, the probe incident angle θ_i was set to 53°. Molecules located at different depths in the sample layer are excited and emit signal fields with different phases in reflection mode. Thus the signal field in reflection mode gradually shifts in phase as the thickness d grows. (b) Calculated pump-probe signals in reflection mode (red, orange) and transmission mode (blue, purple) induced by unit value of Im[$\chi^{(3)}$] (red, blue solid curves) and Re[$\chi^{(3)}$] (orange, purple dashed curves). Im[$\chi^{(3)}$] gives rise to absorptive band shapes, while Re[$\chi^{(3)}$] yields dispersive band shapes. While transmission mode signal is purely absorptive regardless of the layer's thickness, reflection mode spectra contain a dispersive band shape contribution that depends on the thickness. For very thin films, the signal is essentially absorptive. As the sample thickness increases, the both absorptive and dispersive signals in reflection mode increase until $d \sim 0.2\lambda$.

We can quantitatively describe the method applied to thin films by extending Hansen's method, which calculated reflection and transmission from multi-layers with complex refractive indices, $n_j + ik_j$.[44] The pump pulse in Figure 5(a) alters the thin film layer's (second layer's) index from $n_2 + ik_2$ to $(n_2 + \Delta n_2) + i(k_2 + \Delta k_2)$, which changes the reflectivity and transmissivity of the probe beam. These changes are the pump-probe signals. In the supplementary material, we show how Δn_2 and Δk_2 are related to Re[$\chi^{(3)}$] and Im[$\chi^{(3)}$], and how they affect the observed pump-probe signals. In the following, we assume that k_2 and $|\chi^{(3)}|$ are significantly smaller than 1. In this regime, Re[$\chi^{(3)}$] and Im[$\chi^{(3)}$] each contribute linearly to the pump-probe signal.

Note that the values of the imaginary and real susceptibilities depend on the probe's optical frequency, ω. The overall line shapes (frequency dependence) of the reflection

and transmission mode signals are

$$S_{\text{refl.}}(\omega) = C^{\text{abs.}}_{\text{refl.}} \times \text{Im}[\chi^{(3)}(\omega)] + C^{\text{disp.}}_{\text{refl.}} \times \text{Re}[\chi^{(3)}(\omega)], \quad (1)$$

$$S_{\text{trans.}}(\omega) = C^{\text{abs.}}_{\text{trans.}} \times \text{Im}[\chi^{(3)}(\omega)] + C^{\text{disp.}}_{\text{trans.}} \times \text{Re}[\chi^{(3)}(\omega)], \quad (2)$$

where $C^{\text{abs.}}_{\text{refl.}}$, $C^{\text{disp.}}_{\text{refl.}}$, $C^{\text{abs.}}_{\text{trans.}}$, and $C^{\text{disp.}}_{\text{trans.}}$ depend on the thickness of the layer. Figure 5(b) plots the calculated reflection/transmission pump-probe signals, for the geometry in Figure 5(a), induced by unit absorptive ($\text{Im}[\chi^{(3)}]$) and dispersive ($\text{Re}[\chi^{(3)}]$) third-order susceptibilities. These correspond to $C^{\text{abs.}}_{\text{refl.}}$, $C^{\text{disp.}}_{\text{refl.}}$, $C^{\text{abs.}}_{\text{trans.}}$, and $C^{\text{disp.}}_{\text{trans.}}$ in Eqs. (1) and (2).

In Figure 5(b), the signals are plotted with respect to the layer's thickness (d) normalized by the probe/signal wavelength (λ). The calculations are performed at an angle of 53°, which is approaching the Brewster's angle. In a standard transmission mode, the small absorptive signal grows linearly in amplitude with increasing thickness and the dispersive signal is zero, i.e., the signal is purely absorptive regardless of the thickness. The reflection mode signal behaves differently. As the sample thickness increases, the absorptive signal increases when the thickness is significantly smaller than the wavelength. In addition, there is a growing contribution from the dispersive signal. When the thickness reaches a significant fraction of the wavelength, both the absorptive and dispersive signal amplitudes start decaying ($d \sim 0.2 \times \lambda$). Further increase in the film thickness leads to the oscillation in both the absorptive and dispersive signals' amplitudes. When the thickness is less than $d \sim 0.3 \times \lambda$, these amplitudes are substantially larger than the transmission mode signal.

Note that Figure 5(b) displays the absolute amplitudes of the reflection/transmission mode signals. To discuss the enhancement factor in the reflection mode, consider an experiment conducted at $\lambda = 5\ \mu$m on a film that is $d = 100$ nm thick as an example. This thickness would be the first tick mark past zero on the horizontal axis of Figure 5(b) ($d/\lambda = 0.02$). At this wavelength and thickness, the dispersive contribution is negligibly small. For the 53° angle used in the plot, the reflected signal is a factor of 30 greater than the transmitted signal. When the incident angle is instead set to 54°, which is closer to the Brewster's angle $\theta_B = 54.5°$, the enhancement is a factor of 90. Thus the near-Brewster's angle reflection geometry enhances a signal from a film with finite thickness as well as from a monolayer discussed in Sections II A and II B.

As shown above, when the reflection mode pump-probe geometry is applied to a thin film, the line shape is affected by a dispersive contribution. This is indeed not an issue in a simple pump-probe experiment because the dispersive contribution does not affect measurements of the vibrational lifetime or orientational relaxation. However, in a 2D IR experiment, which measures spectral diffusion by examining the T_w dependence of the 2D line shape, a dispersive contribution changes the line shape. For a monolayer or very thin films, the dispersive contribution is essentially zero, as experimentally verified in Figure 3. The question arises as to whether spectral diffusion can be measured for thicker films that have a significant dispersive contribution to the 2D line shape.

To quantitatively evaluate distortions in 2D IR band shapes caused by the dispersion signals, we calculated 2D IR spectra in transmission/reflection modes with various layer thicknesses. We assumed that the frequency-frequency correlation function of the vibrational probe in the layer is given by $\langle \delta\omega(0)\delta\omega(t)\rangle = \delta(t)/(3\,\text{ps}) + (10\ \text{cm}^{-1})^2 \times \exp[-t/(30\,\text{ps})]$. The first term on the right hand side produces homogeneous broadening and the second term gives rise to inhomogeneous broadening. The second term is the source of spectral diffusion. The calculation procedure can be found in the supplementary material. Figure 6(a) shows calculated 2D band shapes for 0-1 transition at the waiting time $T_w = 15$ ps. The four spectra in Figure 6(a) are

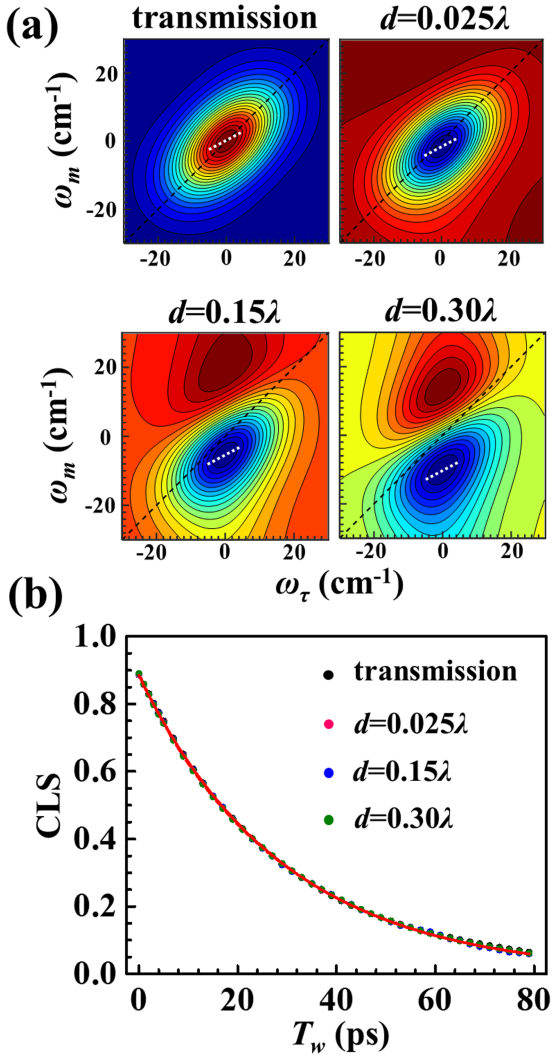

FIG. 6. (a) Simulated 2D IR spectra at $T_w = 15$ ps for the FFCF given in the main text acquired with transmission mode (left top panel) and reflection mode with $\theta_i = 53°$ for three film thicknesses, d. The spectra show only 0-1 transition. For the thinnest sample, $d = 0.025\lambda$, the spectrum is almost purely absorptive. For the thicker samples, the dispersive contribution is large, and the nodes are observed in the middle of the bands. The white dotted lines are the center lines acquired around local maximum or minimum. (b) CLS decays obtained from a series of simulated 2D IR spectra in the transmission mode (black points) and for three thicknesses in the reflection mode (colored points). The calculated points are virtually identical so they are on top of each other and are not separately discernable. In spite of the dispersive band shape contributions for the thicker films, reflection mode 2D spectra yield identical CLS decays as the transmission mode.

different in the acquisition mode (transmission or reflection) and the samples' layer thicknesses. In the transmission mode, the 2D spectrum is purely absorptive regardless of the layer's thickness. Because only the 0-1 band is calculated, there is a single peak. For $d = 0.025\lambda$ in the reflection mode, the dispersive contribution is negligible (see Figure 5(b)), and the band shape is virtually the same as the transmission spectrum. However, as the thickness is increased, the dispersive contribution becomes significant, and the band shape develops nodes in the middle of the 2D bands. At $d = 0.30\lambda$, the band is mainly dispersive.

Nonetheless, all the spectra in Figure 6(a) have well defined local minima or maxima, around which CLS can be calculated. The center lines are the dotted white lines shown for the four spectra in Figure 6(a). In spite of the very different appearance of the band shapes, the center lines for the four spectra in Figure 6(a) yielded identical values of the slope, ~0.525. The 2D spectra were calculated for varieties of T_w and the CLS decays were determined. The results are given in Figure 6(b). The differences among these four decays are undetectable, so much so that it is difficult to discern that there are four overlapping sets of points. The solid curve in Figure 6(b) is a single exponential fit to the points. All of them decay with the time constant of 29.3 ps, missing the correct FFCF decay time constant of 30 ps only by ~2%. (This small error may have arisen from the calculation of the spectra or the determination of the center line slopes, but it is the same for all of the model calculations.) Therefore, while the 2D IR band shape contains a dispersive feature that depends on the thickness of the layer, the dynamical information is maintained and successfully recovered by the CLS method. This is another example showing the robustness of the CLS method as a tool to extract spectral diffusion dynamics from 2D band shapes.[42,43,45]

Overall, when 2D IR spectra are acquired in the near-Brewster's angle reflection pump-probe geometry, (1) while the band shape appears to be distorted (Figure 6(a)), the CLS values and decays are conserved regardless of the thickness (Figure 6(b)), and (2) the absorptive or dispersive signal amplitudes grow until the thickness reaches $d \sim 0.3\lambda$ (Figure 5(b)). Therefore, for an infrared experiment with $\lambda = 5\ \mu$m, the reflection geometry should be readily applicable if the layer thickness is less than ~1 μm, and a significant signal enhancement will be achieved.

III. CONCLUDING REMARKS

In this report, we have demonstrated that the near-Brewster's angle reflection pump-probe geometry enhances the detection of the nonlinear infrared signal from the monolayer by almost two orders of magnitude, compared with the conventional transmission pump-probe signal. For a monolayer that is much thinner than the wavelength of light used in the experiment, the band shapes are purely absorptive. The method was applied to a C_{11} alkyl monolayer, which is bound to an SiO_2 substrate and functionalized with a metal carbonyl head group. Measurements of the signal modulation as a function of incident angle near the Brewster's angle showed increasing enhancement as the Brewster's angle was approached (Figure 2). Calculations of the angle dependence of the enhancement and the experimental data were in quantitative agreement (Figure 1(c)).

Spectral diffusion data acquired from the alkyl monolayer gave results that were consistent with previous measurements using the transmission BOXCARS geometry. However, the signal-to-noise ratio with the reflection pump-probe geometry was so much greater that it was possible to determine that the spectral diffusion is described by a biexponential function. The high data quality and the longer time range offered a more detailed determination of the functional form of the decay. Note that the waiting time T_w dependence of the signal amplitude in this geometry is identical to the one measured in the BOXCARS geometry with all parallel polarizations. Some of the enhancement techniques, such as a polarization grating configuration, accelerate the signal decay rate if there is an in-plane reorientation of the molecules.[46] The near-Brewster's angle reflection pump-probe geometry demonstrated here is thus particularly advantageous in terms of tracking the dynamics over a wide temporal range if there is significant orientational relaxation.

The theoretical framework was developed to describe the enhancement in the same geometry for three-dimensionally isotropic films with finite thickness. Detailed calculations for thin films showed that similar enhancements that were observed for the monolayer will also occur for thin films. It was determined that for thin films, in addition to the absorptive contribution to the signal, the dispersive contribution will occur as the film becomes thicker (Figure 5(b)). For films thinner than $\sim 0.02\lambda$, the dispersive contribution is negligible. For thicker films, 2D IR spectra will display a band shape that is a combination of the absorption and dispersive shapes. However, detailed model calculations showed that the center line slope (CLS) method still extracts the desired frequency-frequency correlation function from the data, regardless of the magnitude of the dispersive contribution to the 2D band shapes. Therefore, the method can be readily extended to thin film samples.

The method should make it possible to study a wide variety of samples that were previously inaccessible to ultrafast nonlinear experiments. While here we studied a monolayer on a transparent substrate to quantitatively evaluate the enhancement factor, the method is applicable as long as the supporting substrate is dielectric; the substrate does not have to be transparent and can be dissipative. Therefore the dynamics at a variety of interfaces can be studied in this geometry. Finally, it is important to note that while the experiments and calculations presented here dealt with IR nonlinear spectroscopy, all of the considerations apply equally to experiments in the visible or ultraviolet spectroscopic regions.

SUPPLEMENTARY MATERIAL

See supplementary material for (A) calculation for incident angle dependence of pump-probe signal, (B) experimental details for pump-probe spectroscopy and two-dimensional infrared spectroscopy, (C) enhanced absorption, and (D) calculations for the thickness dependence of the pump-probe signal and the two-dimensional band shape.

ACKNOWLEDGMENTS

This material is based upon work supported by the Air Force Office of Scientific Research under AFOSR Award No. FA9550-16-1-0104.

[1] D. M. Jonas, Annu. Rev. Phys. Chem. **54**, 425 (2003).
[2] G. S. Engel, T. R. Calhoun, E. L. Read, T.-K. Ahn, T. Mančal, Y.-C. Cheng, R. E. Blankenship, and G. R. Fleming, Nature **446**, 782 (2007).
[3] M. D. Fayer, Annu. Rev. Phys. Chem. **60**, 21 (2009).
[4] P. Hamm and M. T. Zanni, *Concepts and Methods of 2D Infrared Spectroscopy* (Cambridge University Press, New York, 2011).
[5] W. Xiong, J. E. Laaser, R. D. Mehlenbacher, and M. T. Zanni, Proc. Natl. Acad. Sci. U. S. A. **108**, 20902 (2011).
[6] J. B. Asbury, T. Steinel, C. Stromberg, S. A. Corcelli, C. P. Lawrence, J. L. Skinner, and M. D. Fayer, J. Phys. Chem. A **108**, 1107 (2004).
[7] J. J. Loparo, S. T. Roberts, and A. Tokmakoff, J. Chem. Phys. **125**, 194521 (2006).
[8] S. Roy, D. Skoff, D. V. Perroni, J. Mondal, A. Yethiraj, M. K. Mahanthappa, M. T. Zanni, and J. L. Skinner, J. Am. Chem. Soc. **138**, 2472 (2016).
[9] J. T. King, M. R. Ross, and K. J. Kubarych, Phys. Rev. Lett. **108**, 157401 (2012).
[10] D. B. Wong, C. H. Giammanco, E. E. Fenn, and M. D. Fayer, J. Phys. Chem. B **117**, 623 (2013).
[11] Z. Ren, T. Brinzer, S. Dutta, and S. Garrett-Roe, J. Phys. Chem. B **119**, 4699 (2015).
[12] S. Woutersen, Y. Mu, G. Stock, and P. Hamm, Proc. Natl. Acad. Sci. U. S. A. **98**, 11254 (2001).
[13] P. Mukherjee, I. Kass, I. T. Arkin, and M. T. Zanni, Proc. Natl. Acad. Sci. U. S. A. **103**, 3528 (2006).
[14] M. C. Thielges and M. D. Fayer, Acc. Chem. Res. **45**, 1866 (2012).
[15] S.-H. Shim and M. T. Zanni, Phys. Chem. Chem. Phys. **11**, 748 (2009).
[16] L. P. DeFlores, R. A. Nicodemus, and A. Tokmakoff, Opt. Lett. **32**, 2966 (2007).
[17] S. H. Shim, D. B. Strasfeld, Y. L. Ling, and M. T. Zanni, Proc. Natl. Acad. Sci. U. S. A. **104**, 14197 (2007).
[18] S. K. K. Kumar, A. Tamimi, and M. D. Fayer, J. Chem. Phys. **137**, 184201 (2012).
[19] W. Rock, Y.-L. Li, P. Pagano, and C. M. Cheatum, J. Phys. Chem. A **117**, 6073 (2013).
[20] S. Park, K. Kwak, and M. D. Fayer, Laser Phys. Lett. **4**, 704 (2007).
[21] D. E. Rosenfeld, Z. Gengeliczki, B. J. Smith, T. D. P. Stack, and M. D. Fayer, Science **334**, 634 (2011).
[22] C. Yan, R. Yuan, W. C. Pfalzgraff, J. Nishida, L. Wang, T. E. Markland, and M. D. Fayer, Proc. Natl. Acad. Sci. U. S. A. **113**, 4929 (2016).
[23] J. P. Kraack, D. Lotti, and P. Hamm, J. Phys. Chem. Lett. **5**, 2325 (2014).
[24] J. P. Kraack, A. Kaech, and P. Hamm, J. Phys. Chem. C **120**, 3350 (2016).
[25] O. Selig, R. Siffels, and Y. Rezus, Phys. Rev. Lett. **114**, 233004 (2015).
[26] J. Burschka, N. Pellet, S.-J. Moon, R. Humphry-Baker, P. Gao, M. K. Nazeeruddin, and M. Grätzel, Nature **499**, 316 (2013).
[27] N. J. Jeon, J. H. Noh, Y. C. Kim, W. S. Yang, S. Ryu, and S. I. Seok, Nat. Mater. **13**, 897 (2014).
[28] R. A. Dluhy, J. Phys. Chem. **90**, 1373 (1986).
[29] H. Brunner, U. Mayer, and H. Hoffmann, Appl. Spectrosc. **51**, 209 (1997).
[30] Y. Nishikawa, K. Fujiwara, K. Ataka, and M. Osawa, Anal. Chem. **65**, 556 (1993).
[31] W. Xiong and M. T. Zanni, Opt. Lett. **33**, 1371 (2008).
[32] T. L. Courtney, S. D. Park, R. J. Hill, B. Cho, and D. M. Jonas, Opt. Lett. **39**, 513 (2014).
[33] J. Nishida, C. Yan, and M. D. Fayer, J. Phys. Chem. C **118**, 523 (2014).
[34] J. Nishida, C. Yan, and M. D. Fayer, J. Am. Chem. Soc. **138**, 14057 (2016).
[35] E. Hecht, *Optics* (Addison-Wesley, San Francisco, 2002).
[36] T. F. Heinz, *Modern Problems in Condensed Matter Sciences*, Nonlinear Surface Electromagnetic Phenomena (Elsevier, 1991), Vol. 29, p. 353.
[37] X. Zhuang, P. B. Miranda, D. Kim, and Y. R. Shen, Phys. Rev. B **59**, 12632 (1999).
[38] Y. Shen, Annu. Rev. Phys. Chem. **40**, 327 (1989).
[39] S. Yamaguchi, H. Hosoi, M. Yamashita, P. Sen, and T. Tahara, J. Phys. Chem. Lett. **1**, 2662 (2010).
[40] J. Nishida and M. D. Fayer, J. Chem. Phys. **140**, 144702 (2014).
[41] O. Golonzka, M. Khalil, N. Demirdöven, and A. Tokmakoff, Phys. Rev. Lett. **86**, 2154 (2001).
[42] K. Kwak, S. Park, I. J. Finkelstein, and M. D. Fayer, J. Chem. Phys. **127**, 124503 (2007).
[43] K. Kwak, D. E. Rosenfeld, and M. D. Fayer, J. Chem. Phys. **128**, 204505 (2008).
[44] W. N. Hansen, J. Opt. Soc. Am. **58**, 380 (1968).
[45] Q. Guo, P. Pagano, Y.-L. Li, A. Kohen, and C. M. Cheatum, J. Chem. Phys. **142**, 212427 (2015).
[46] A. Tokmakoff, J. Chem. Phys. **105**, 1 (1996).